

A theoretical model for linear and nonlinear spectroscopy of plexcitons

Chenghong Huang,^{1,2} Shuming Bai,^{1,2, a)} and Qiang Shi^{1,2, b)}

¹⁾*Beijing National Laboratory for Molecular Sciences, State Key Laboratory for Structural Chemistry of Unstable and Stable Species, Institute of Chemistry, Chinese Academy of Sciences, Zhongguancun, Beijing 100190, China*

²⁾*University of Chinese Academy of Sciences, Beijing 100049, China*

We present a theoretical model to investigate the dynamics and spectroscopic properties of a plexciton system consisting of a molecular exciton coupled to a single short-lived plasmonic mode. The exciton is described as a two-level system (TLS), while the plasmonic mode is treated as a dissipative harmonic oscillator. The hierarchical equations of motion method is employed to simulate energy transfer dynamics, absorption spectra, and two-dimensional electronic spectra (2DES) of the system across a range of coupling strengths. It is shown that increasing the exciton-plasmon coupling strength drives a transition in the absorption spectra from an asymmetric Fano line shape to a Rabi splitting pattern, while coupling the TLS to intramolecular vibrational modes reduces the central dip of the absorption spectra and makes the line shape more symmetric. The simulated 2DES exhibit distinct features compared to those of a coupled molecular dimer, highlighting the unique nonlinear response of plexciton systems. In addition, a “breathing mode” pattern observed in the strong coupling regime can serve as a direct evidence of Rabi oscillation.

^{a)}Electronic mail: baishuming@iccas.ac.cn

^{b)}Electronic mail: qshi@iccas.ac.cn

I. INTRODUCTION

Plasmons are collective oscillations of electrons in metals or metallic nanoparticles.^{1,2} They produce highly localized electromagnetic fields that enable strong interactions with nearby excitons, which are bound states of electrons and holes in molecules or semiconductors. When plasmons and excitons are brought close together, they can couple to form hybrid states called plexcitons. Plexcitons combine the tight field confinement of plasmons with the discrete energy levels of excitons, resulting in unique optical properties suitable for applications ranging from solar cells to quantum information technologies.^{3–8}

The exciton-plasmon coupled systems can be classified by their individual damping rate and how fast energy exchanges between them.^{8,9} In the weak coupling regime, the plasmon damping rate is significantly higher than that of the energy exchange between the exciton and plasmon. The behavior of exciton is thus minimally influenced by plasmon in such cases, while the emission rate of the quantum emitter can be enhanced due to the Purcell effect,¹⁰ which have been observed in various systems.^{11–14}

In the strong coupling regime, where the energy exchange rate between the exciton and plasmon exceeds their respective damping rates, the hybrid plexciton states are formed, resulting in the characteristic Rabi splitting.^{15,16} This regime can be achieved by carefully selecting the metal materials, precisely controlling the shape and size of the metal nanoparticles, and optimizing the coupling mechanisms between the emitters and plasmons.

In recent decades, many experiments have demonstrated peak splitting in linear spectroscopy for quantum emitters strongly coupled to plasmonic nanoparticles. For instance, Zengin et al. studied TDBC J-aggregates both as thin layers surrounding a silver nanorod and as sheets attached to a silver nanoprism, observing peak splittings of 976 cm^{-1} and 2880 cm^{-1} in dark-field scattering spectra.^{17,18} Chikkaraddy et al. reported strong coupling of small numbers of dye molecules to plasmonic nanocavities made of gold nanoparticles on gold mirrors at room temperature.¹⁹ Santhosh et al. observed vacuum Rabi splitting in a single quantum dot coupled to plasmonic cavities formed by a silver nanoparticle dimer, with peak splitting comparable to that of multi-emitter plasmonic systems.²⁰ Two-dimensional electronic spectroscopy (2DES) has also been applied to both isolated plasmonic and plexcitonic systems to investigate coherent interactions and population dynamics, revealing the time scales of various energy relaxation pathways^{21,22}.

Theoretical models and simulations are essential to understand the energy pathways and the spectroscopy signals observed in experiments.^{17,18,20,21,23–25} Based on the classical model of coupled harmonic oscillators,²⁶ Faucheaux *et al.* investigated the transition in scattering line shape from Rabi splitting to Fano interference by increasing the damping rate of the plasmonic oscillator.²⁷ Quantum models have also been developed. Manjavacas *et al.* simulated the absorption spectra of a two level system coupled to a nanoparticle plasmon dimer using Zubarev’s Green functions.²⁸ Tomasz and coworkers modeled the photoabsorption spectra of metal nanoparticle dimers coupled to organic conjugated molecules using first-principle calculations.^{29,30}

Non-Hermitian effective Hamiltonian approaches,^{31–33} which include the damping of both the plasmon and exciton while considering their coupling, have become increasingly popular due to their clear physical picture and low computational cost compared to full quantum simulations. Varguet *et al.* used this approach to investigate a two-level system coupled to a multi-mode localized surface plasmon, revealing a new hybrid energy diagram and Rabi splitting in the polarization spectrum³³. Finkelstein-Shapiro *et al.* modeled the linear absorption and 2DES of plexcitons, providing insights into the time scales of different relaxation pathways²¹. In a subsequent work, they demonstrated how the linear spectra and shape symmetries in 2DES change across weak and strong coupling conditions.³⁴

In this work, we present a theoretical model of a plexciton system consisting of a molecular exciton coupled to a single plasmonic mode. The exciton is described as a two-level system (TLS), while the plasmonic mode is modeled as a dissipative harmonic oscillator. The TLS can also be coupled to intramolecular vibrational modes to account for electronic-vibrational coupling in the exciton. The dynamics and spectroscopic signals of this plexciton system are then simulated using the hierarchical equations of motion (HEOM) method.^{35–37} The absorption spectra are calculated by deriving the dipole autocorrelation functions, and the effects of exciton-plasmon coupling strength and intramolecular vibrational modes are analyzed. To investigate the nonlinear response of the plexciton system, two-dimensional electronic spectra (2DES) are simulated through direct calculations of the system’s response to external laser pulses.³⁸ The 2DES for different coupling strengths are presented, along with their relationship to field-driven exciton dynamics.

The remaining sections of this paper are organized as follows. In Sec. II, we introduce the model Hamiltonian for the plexciton system, provide a brief overview of the HEOM

method, and describe the approaches used to calculate the linear absorption spectra and 2DES. In Sec. III, we present the results for the absorption spectra and 2DES under various conditions. Finally, conclusions and discussions are made in Sec. IV.

II. THEORY

A. Model Hamiltonian

We consider the molecular exciton as a TLS, and describe the plasmonic mode as a group of harmonic oscillator modes, which is also equivalent to a single harmonic oscillator mode coupled to a dissipative bath.³⁹ The Hamiltonian of the total system is given by:

$$H = H_e + H_p + H_{e-p} . \quad (1)$$

H_e describes the electronic degrees of freedom (DOFs) of the exciton with

$$H_e = \begin{pmatrix} 0 & 0 \\ 0 & \omega_0 \end{pmatrix} , \quad (2)$$

where ω_0 is the transition energy of the TLS. H_p is the Hamiltonian of harmonic oscillator bath used to describe the plasmon mode, and is given by

$$H_p = \sum_{j=1}^{N_b} \left(\frac{p_j^2}{2} + \frac{1}{2} \omega_j^2 x_j^2 \right) , \quad (3)$$

where the N_b is the number of the bath modes, x_j and p_j are the position and momentum of the j th harmonic oscillator bath mode with frequency ω_j .

The exciton-plasmon coupling H_{e-p} is assumed to arise from dipole-dipole coupling between the TLS and the plasmon,

$$H_{e-p} = -\alpha \sum_{j=1}^{N_b} c_j x_j \otimes \sigma_x = -\alpha F \otimes \sigma_x , \quad (4)$$

where the collective bath coordinate $F = \sum_{j=1}^{N_b} c_j x_j$ describes the dipole moment operator of the plasmon modes, $\sigma_x = |0\rangle\langle 1| + |1\rangle\langle 0|$ is the Pauli matrix associated with the transition dipole of the TLS, α is a dimensionless coefficient. The spectral density $J(\omega)$ is defined as:

$$J(\omega) = \frac{\pi}{2} \sum_{j=1}^{N_b} \frac{c_j^2}{\omega_j} \delta(\omega - \omega_j) . \quad (5)$$

The autocorrelation function of the collective bath coordinates F is then given by:

$$C(t) = \frac{1}{Z_B} \text{Tr}(e^{-\beta H_p} e^{iH_p t} F e^{-iH_p t} F) = \frac{1}{\pi} \int_{-\infty}^{\infty} d\omega \frac{e^{-i\omega t} J(\omega)}{1 - e^{-\beta\omega}} , \quad (6)$$

where we have extended the definition of the spectral density to $\omega < 0$, with $J(-\omega) = -J(\omega)$.

In this study, we employ a Lorentzian type spectral density to describe the damped harmonic oscillator:^{39–41}

$$J(\omega) = 4\lambda_0 \frac{\gamma\Omega^2\omega}{(\Omega^2 - \omega^2)^2 + 4\gamma^2\omega^2} , \quad (7)$$

or its equivalent form:^{41–43}

$$J(\omega) = \frac{p_0\omega}{[(\omega + \omega_p)^2 + \gamma^2][(\omega - \omega_p)^2 + \gamma^2]} , \quad (8)$$

with the relationships of $\Omega^2 = \omega_p^2 + \gamma^2$ and $p_0 = 4\lambda_0\Omega^2\gamma$. Here, γ^{-1} describes relaxation time of the under damped plasmonic mode, ω_p is the oscillating frequency, and λ_0 is the renormalization energy.

The dipole moment operator consists of contributions from both the TLS and the collective bath mode for the plasmons, and is given by:

$$\mu = \mu_{\text{TLS}}\sigma_x + \frac{\mu_P}{\lambda_0}F , \quad (9)$$

where μ_{TLS} and μ_P are constants related to the transition dipole moment of the TLS and plasmon mode. Since both F and λ_0 have units of energy, μ_{TLS} and μ_P also have the same units.

B. HEOM

In the HEOM formalism, the bath correlation function in Eq.(6) is first written into a sum of exponential decaying functions in time:

$$C(t) = \sum_{k=0}^{K-1} c_k e^{-\gamma_k t} . \quad (10)$$

In this work, the barycentric spectral decomposition (BSD) method^{44,45} is used to obtain the exponential decomposition of the bath correlation function. This approach has been demonstrated to handle general forms of spectral densities and low-temperature conditions with high accuracy and efficiency.^{44,45}

The BSD methods works in the frequency domain. The product of the spectral density $J(\omega)$ and the Bose function $1/(1 - e^{-\beta\omega})$ in Eq. (6) is first fitted by a summation of fractions:

$$\frac{J(\omega)}{1 - e^{-\beta\omega}} = \sum_k \frac{r_k}{\omega - p_k} . \quad (11)$$

The residuals $\{r_k\}$ and poles $\{p_k\}$ are then used for the exponential decomposition of the bath correlation function:

$$C(t) = \frac{1}{\pi} \int_{-\infty}^{\infty} d\omega \frac{e^{-i\omega t} J(\omega)}{1 - e^{-\beta\omega}} = -2i \sum_k r_k e^{-ip_k t} . \quad (12)$$

It is noticed that, the Cauchy contour integral in Eq. (12) requires only the poles p_k s with a negative imaginary part in the summation. The complex coefficients and decaying constants in Eq.(10) are thus given by:

$$c_k = -2ir_k, \quad \gamma_k = ip_k . \quad (13)$$

By applying the dynamics filtering approach with the renormalized auxiliary density operators (ADOs),⁴⁶

$$\tilde{\rho}_{\mathbf{m},\mathbf{n}} = \frac{\rho_{\mathbf{m},\mathbf{n}}}{\prod_k \sqrt{|c_k|^{m_k} m_k!} \sqrt{|c_k^*|^{n_k} n_k!}} , \quad (14)$$

the formal exact HEOM are then given by:

$$\begin{aligned} \frac{d}{dt} \tilde{\rho}_{\mathbf{m},\mathbf{n}} = & - \left(i\mathcal{L} + \sum_k m_k \gamma_k + \sum_k n_k \gamma_k^* \right) \tilde{\rho}_{\mathbf{m},\mathbf{n}} + i \sum_k \sqrt{(m_k + 1)c_k} \left[\alpha\sigma_x, \tilde{\rho}_{\mathbf{m}_k^+, \mathbf{n}} \right] \\ & + i \sum_k \sqrt{(n_k + 1)c_k^*} \left[\alpha\sigma_x, \tilde{\rho}_{\mathbf{m}, \mathbf{n}_k^+} \right] + i \sum_k \sqrt{m_k c_k} \alpha\sigma_x \tilde{\rho}_{\mathbf{m}_k^-, \mathbf{n}} + i \sum_k \sqrt{n_k c_k^*} \tilde{\rho}_{\mathbf{m}, \mathbf{n}_k^-} \alpha\sigma_x . \end{aligned} \quad (15)$$

where $\mathcal{L}\tilde{\rho} = [H_e, \tilde{\rho}]$ is the Liouville operator. The subscripts \mathbf{n} denotes the set of indices $\mathbf{n} = \{n_1, n_2, \dots\}$, and \mathbf{n}_k^\pm differs from \mathbf{n} only by changing the specified n_k to $n_k \pm 1$. The $\rho_{\mathbf{0},\mathbf{0}}$ term with $\mathbf{0} = \{0, 0, \dots\}$ is the system reduced density operator (RDO), while the other $\rho_{\mathbf{m},\mathbf{n}}$ terms are the ADOs. The ADOs contain important information on the system-bath correlations,⁴⁷⁻⁵⁰ which will be shown later in our calculations of the dipole autocorrelation functions and the field-induced polarization.

C. Linear Absorption Spectra

The linear absorption spectra of the plexciton system are obtained by the Fourier transform of dipole autocorrelation function:⁵¹

$$I(\omega) \propto \frac{1}{2\pi} \int_{-\infty}^{\infty} dt e^{i\omega t} \langle \mu(t) \mu(0) \rangle , \quad (16)$$

where

$$\langle \mu(t) \mu(0) \rangle = \text{Tr}[e^{iHt} \mu e^{-iHt} \mu \rho_{eq}] = \text{Tr}[\mu e^{-iHt} \mu \rho_{eq} e^{iHt}] , \quad (17)$$

where ρ_{eq} is the equilibrium density operator $\rho_{eq} = e^{-\beta H} / \text{Tr} e^{-\beta H}$ ($\beta = 1/k_B T$ is the inverse temperature).

The calculation process differs slightly from our previous work on molecular systems^{52,53} due to the dipole operator defined in Eq. (9), which includes not only the system (TLS) part but also contributions from the bath. As a result, the initial state used for real-time propagation with the HEOM is given by:^{47,49,50}

$$\rho_{\mathbf{m},\mathbf{n}}(t=0, \mu) = \mu_{\text{TLS}} \sigma_x \rho_{\mathbf{m},\mathbf{n}}^{eq} + \frac{\mu_P}{\lambda_0} \sum_k \left(\rho_{\mathbf{m}_k^+, \mathbf{n}}^{eq} + \rho_{\mathbf{m}, \mathbf{n}_k^+}^{eq} + m_k c_k \rho_{\mathbf{m}_k^-, \mathbf{n}}^{eq} \right) , \quad (18)$$

and after renormalization in Eq.(14), it becomes

$$\tilde{\rho}_{\mathbf{m},\mathbf{n}}(t=0, \mu) = \mu_{\text{TLS}} \sigma_x \tilde{\rho}_{\mathbf{m},\mathbf{n}}^{eq} - \frac{\mu_P}{\lambda_0} \sum_k \left(\sqrt{(m_k + 1)} c_k \tilde{\rho}_{\mathbf{m}_k^+, \mathbf{n}}^{eq} + \sqrt{(n_k + 1)} c_k^* \tilde{\rho}_{\mathbf{m}, \mathbf{n}_k^+}^{eq} + \sqrt{m_k c_k} \tilde{\rho}_{\mathbf{m}_k^-, \mathbf{n}}^{eq} \right) , \quad (19)$$

The minus sign in the above equation is due to the convention in defining the ADOs.⁴⁷

After obtaining the RDO/ADOs $\rho_{\mathbf{m},\mathbf{n}}(t, \mu)$ at time t through the propagation of the HEOM, we can calculate the auto-dipole correlation as:^{49,50}

$$\begin{aligned} \langle \mu(t) \mu(0) \rangle &= \mu_{\text{TLS}} \sigma_x \text{Tr} [\rho_{\mathbf{0},\mathbf{0}}(t, \mu)] - \frac{\mu_P}{\lambda_0} \text{Tr} \left[\sum_k [\rho_{\mathbf{1},\mathbf{0}}^k(t, \mu) + \rho_{\mathbf{0},\mathbf{1}}^k(t, \mu)] \right] \\ &= \mu_{\text{TLS}} \sigma_x \text{Tr} [\tilde{\rho}_{\mathbf{0},\mathbf{0}}(t, \mu)] - \frac{\mu_P}{\lambda_0} \text{Tr} \left[\sum_k \left[\sqrt{c_k} \tilde{\rho}_{\mathbf{1},\mathbf{0}}^k(t, \mu) + \sqrt{c_k^*} \tilde{\rho}_{\mathbf{0},\mathbf{1}}^k(t, \mu) \right] \right] , \end{aligned} \quad (20)$$

where $\rho_{\mathbf{0},\mathbf{0}}(t, \mu)$ is the RDO, $\rho_{\mathbf{1},\mathbf{0}}(t, \mu)$ s and $\rho_{\mathbf{0},\mathbf{1}}(t, \mu)$ s are the first-tier ADOs.

D. 2DES

When calculating 2DES, we employ the previously developed method to directly calculate molecular responses with explicit laser fields,⁵⁴⁻⁵⁶ which naturally takes account into the

effects of finite laser pulse durations. To this end, the Hamiltonian describing the interaction between the laser field and the plexciton system is defined as:

$$H_{int} = -\mu E(t) = -\mu_{\text{TLS}} E(t) \sigma_x - \frac{\mu_{\text{P}}}{\lambda_0} E(t) F \quad , \quad (21)$$

where μ represents the total dipole operator of the plexciton system. The laser pulses are modeled as classical electromagnetic fields, with the electric field expressed as:

$$E(t) = \sum_{i=1}^3 E_i(t) e^{-i(\omega_i t - \mathbf{k}_i \cdot \mathbf{r})} + c.c. \quad , \quad (22)$$

where the summation accounts for the three laser pulses used in the 2DES experiment.

The total Hamiltonian, obtained by combining Eqs. (1) and (21), is given by:

$$H_T(t) = [H_e - \mu_{\text{TLS}} \sigma_x E(t)] + H_p - \left[\alpha \sigma_x + \frac{\mu_{\text{P}}}{\lambda_0} E(t) \right] \otimes F \quad . \quad (23)$$

The above Hamiltonian contains the interaction of the external field and the bath DOFs, and the corresponding HEOM have been obtained previously in Refs.^{49,57}:

$$\begin{aligned} \frac{d}{dt} \tilde{\rho}_{\mathbf{m},\mathbf{n}} = & - \left(i\mathcal{L}(t) + \sum_k m_k \gamma_k + \sum_k n_k \gamma_k^* \right) \tilde{\rho}_{\mathbf{m},\mathbf{n}} + i \sum_k \sqrt{(m_k + 1)c_k} \left[\alpha \sigma_x + \frac{\mu_{\text{P}}}{\lambda_0} E(t), \tilde{\rho}_{\mathbf{m}_k^+, \mathbf{n}} \right] \\ & + i \sum_k \sqrt{(n_k + 1)c_k^*} \left[\alpha \sigma_x + \frac{\mu_{\text{P}}}{\lambda_0} E(t), \tilde{\rho}_{\mathbf{m}, \mathbf{n}_k^+} \right] + i \sum_k \sqrt{m_k c_k} \left[\alpha \sigma_x + \frac{\mu_{\text{P}}}{\lambda_0} E(t) \right] \tilde{\rho}_{\mathbf{m}_k^-, \mathbf{n}} \\ & + i \sum_k \sqrt{n_k c_k^*} \tilde{\rho}_{\mathbf{m}, \mathbf{n}_k^-} \left[\alpha \sigma_x + \frac{\mu_{\text{P}}}{\lambda_0} E(t) \right] \quad . \quad (24) \end{aligned}$$

where $\mathcal{L}(t)\rho = [H_e - \mu_{\text{TLS}} \sigma_x E(t), \rho]$ is the time-dependent Liouville operator.

The total optical polarization induced by the laser pulses is given by:

$$P(t) = \langle \mu \rho(t) \rangle \quad , \quad (25)$$

where the average is taken over all DOFs. This total polarization includes contributions from all orders of interaction with the laser field along different output directions. It is thus necessary to separate the third order rephasing (RP) and non-rephasing (NR) signals from the total polarization.^{38,54,58,59} For this purpose, we adopt the calculation scheme originally developed by Gelin *et al.*, which is based on perturbation theory and employs a combination of auxiliary density operators.³⁸ This approach has been widely applied to simulate third-order spectroscopy signals, including three-pulse photon echo and two-dimensional electronic spectroscopy^{38,56,60–62}.

In this framework, the explicit form of the third-order polarization is:

$$P^{(3)}(t) = \langle \mu[\rho_1(t) - \rho_2(t) - \rho_3(t) - \rho_4(t) + \rho_5(t) + \rho_6(t) + \rho_7(t)] \rangle , \quad (26)$$

the seven auxiliary density operators are defined as:³⁸

$$\begin{aligned} \rho_1(t) &= \rho(E_1(t), E_2(t), E_3(t)), & \rho_2(t) &= \rho(E_1(t), E_2(t), 0), \\ \rho_3(t) &= \rho(E_1(t), 0, E_3(t)), & \rho_4(t) &= \rho(0, E_2(t), E_3(t)), \\ \rho_5(t) &= \rho(E_1(t), 0, 0), & \rho_6(t) &= \rho(0, E_2(t), 0), & \rho_7(t) &= \rho(0, 0, E_3(t)) . \end{aligned} \quad (27)$$

Whenever there is a zero in the above definitions, it indicates that the corresponding laser pulse is omitted in calculating the total electric field. All auxiliary density operators are computed using the time-dependent HEOM in Eq. (24). In order to obtain the 2D spectra, the RP and NR signals are extracted using the phase-matching approach (PMA),⁶³ where a specific component of the laser field is selectively incorporated into the simulation. For instance, when calculating the RP signal along the direction $\mathbf{k}_I = -\mathbf{k}_1 + \mathbf{k}_2 + \mathbf{k}_3$, we use

$$\begin{aligned} E_1(t) &= E_1 e^{-\frac{(t-t_1)^2}{2\sigma^2}} e^{i[\omega_1(t-t_1) - \mathbf{k}_1 \cdot \mathbf{r}]}, \\ E_2(t) &= E_2 e^{-\frac{(t-t_2)^2}{2\sigma^2}} e^{-i[\omega_2(t-t_2) - \mathbf{k}_2 \cdot \mathbf{r}]}, \\ E_3(t) &= E_3 e^{-\frac{(t-t_3)^2}{2\sigma^2}} e^{-i[\omega_3(t-t_3) - \mathbf{k}_3 \cdot \mathbf{r}]} . \end{aligned} \quad (28)$$

For the NR signal associated with $\mathbf{k}_{II} = \mathbf{k}_1 - \mathbf{k}_2 + \mathbf{k}_3$, we have:

$$\begin{aligned} E_1(t) &= E_1 e^{-\frac{(t-t_1)^2}{2\sigma^2}} e^{-i[\omega_1(t-t_1) - \mathbf{k}_1 \cdot \mathbf{r}]}, \\ E_2(t) &= E_2 e^{-\frac{(t-t_2)^2}{2\sigma^2}} e^{i[\omega_2(t-t_2) - \mathbf{k}_2 \cdot \mathbf{r}]}, \\ E_3(t) &= E_3 e^{-\frac{(t-t_3)^2}{2\sigma^2}} e^{-i[\omega_3(t-t_3) - \mathbf{k}_3 \cdot \mathbf{r}]} . \end{aligned} \quad (29)$$

Once the third-order responses for the RP and NR signals are obtained, the 2DES can be calculated by performing a double Fourier transform with respect to the coherence time τ and the detection time t as:^{55,61,64}

$$S(\omega_\tau, T_2, \omega_t) = \text{Re} \int_0^\infty d\tau \int_0^\infty dt' [e^{-i\omega_\tau \tau + i\omega_t t'} \times iP_{rp}(\tau, T_2, t') + e^{i\omega_\tau \tau + i\omega_t t'} \times iP_{nr}(\tau, T_2, t')], \quad (30)$$

where ω_τ is the excitation frequency, ω_t is the detection frequency, $\tau = t_2 - t_1$ is the coherence time, $T_2 = t_3 - t_2$ is the waiting time, $t' = t - t_3$ is the detection time.

III. RESULTS

A. Population dynamics of the coupled system

The above HEOM are then applied to a model consisting of a quantum emitter described by a TLS, and a single dissipative plasmon mode as the harmonic bath. All the simulations are performed at room temperature of 298K. The transition energy of the exciton is $\omega_0 = 15000 \text{ cm}^{-1}$. We also use $\omega_p = 15000 \text{ cm}^{-1}$ in the Lorentzian spectral density in Eq. (7), assuming energy resonance between the emitter and plasmon. The other parameters of Lorentzian spectral density are $\gamma^{-1} = 5 \text{ fs}$ corresponding to fast decay of the plasmon mode.¹ The renormalization energy $\lambda_0 = 0.05 \text{ a.u.}$ ($1.1 \times 10^4 \text{ cm}^{-1}$). By using the equivalence of the TLS-Lorentzian bath model and the TLS-Harmonic oscillator-Ohmic bath model,³⁹ we can calculate the effective coupling between the TLS and the first excited state of the undamped harmonic plasmon mode, which is given by $\Delta = \alpha\sqrt{\lambda_0\Omega}$, where α , λ_0 , and Ω are given in Sec. 2.1. For $\alpha = 0.1$, the coupling constant is $\Delta = 1287 \text{ cm}^{-1}$, which satisfies the condition of the strong-coupling regime.^{65,66} The transition dipole moments for the TLS and plasmon are taken as $\mu_{\text{TLS}} = 1$ and $\mu_{\text{P}} = 10$, respectively.

The excited-state population dynamics of the TLS are obtained for various coupling strengths α and are shown in Fig. 1, where the initial state is a factorized state with the TLS in the excited state and the plasmon mode in the thermal equilibrium. For simplicity, coupling of the TLS to intramolecular vibrational modes is not included. In the case of weak coupling $\alpha = 0.01$, the population dynamics show a slow decay with a time constant of approximately 300 fs. For larger coupling strengths from $\alpha = 0.1$ and $\alpha = 0.2$, the population dynamics exhibit Rabi oscillations, although with rapid decay caused by the short lifetime of the plasmon mode. The $\alpha = 0.05$ case represents an intermediate case.

B. Linear Absorption spectra

The simulated absorption spectra of the TLS-plasmon coupling strength $\alpha = 0.1$ are presented in Fig. 2. The absorption spectra of the plasmon mode is shown in the black dashed line. The broad width of the peak arises from the short lifetime of the plasmon mode. The red dashed line represents the absorption spectra of the isolated TLS. When there is coupling between the TLS and the plasmon mode, we consider two cases: one

where the TLS is not coupled to the intramolecular vibrational DOFs, referred to as the “bare TLS,” and another where the TLS is coupled to the vibrational DOFs that leads to decoherence effects, referred to as the “dissipative TLS”.

In the latter case, to take account into effects of coupling between intramolecular vibrational modes and the electronic transition, we employ a shifted harmonic oscillator model to describe the ground and excited state potential surfaces.^{52,53} In this model, the coupling between the TLS and the vibrational modes is described by a Debye-Drude spectral density.^{52,53}

$$J_D(\omega) = \frac{\eta\gamma_D\omega}{\gamma_D^2 + \omega^2} , \quad (31)$$

with the parameters $\eta = 200 \text{ cm}^{-1}$ and $\gamma_D^{-1} = 40 \text{ fs}$. In Fig. 2, the isolated TLS spectra is enlarged by 50 times for better visualization.

The absorption spectra of the plexciton for $\alpha = 0.1$, without and with coupling to vibrational DOFs are shown in Fig. 2 as blue and green lines, respectively. As discussed earlier, this is a case of strong coupling. The observed peak splitting is 2723 cm^{-1} for the case of bare TLS, which is consistent with the period of the Rabi oscillations in the population dynamics, as shown in Fig. 1. In the spectra with coupling to the vibrational modes, the peak splitting is of a similar value. In the case of the bare TLS (blue line), the dip between the two absorption peaks is very deep, reaching close to the ω -axis. On the other hand, the dip in the presence of TLS-vibrational coupling (green curve) is shallower. Additionally, the lower and upper energy peaks are more symmetric when there is coupling to the vibrational modes.

The influence of the TLS-plasmon coupling strength on the absorption line shape is shown in Fig. 3, where the upper panel presents the results for the bare TLS and the lower panel shows results for the TLS coupled with vibrational modes. The dimensionless coupling factor α ranges from weak coupling ($\alpha = 0.01$) to strong coupling ($\alpha = 0.15$). For $\alpha = 0.01$, the absorption spectrum exhibits a sharp asymmetric dip, characteristic of the Fano line shape (black line, upper panel). As the TLS-plasmon coupling strength increases, the line shape evolves into an asymmetric double peak. This transition from Fano line shape to peak splitting caused by Rabi oscillation is consistent with previous analysis based on the classical model.²⁷

The effects of coupling to intramolecular vibrational modes on the absorption line shape

are clearly visible in the lower panel of Fig. 3. In the upper panel, the central dips are very deep, almost reaching the ω -axis, whereas in the lower panel, the dips are shallower and vary with the TLS-plasmon coupling strength. This effect is more pronounced for weak to intermediate coupling strengths. Notably, in the $\alpha = 0.01$ case, the dip completely vanishes, resulting in a single peak that is distinctly different from the line shape in the upper panel. This likely explains that the Fano line shape is rarely observed in the weak coupling regime: coupling to the vibrational modes is always present and introduces decoherence to the TLS.⁶⁷ For all spectra that retain the double peak structure, the line width and the amplitude of the peak splitting remain essentially the same, although the peaks become more symmetric in the presence of coupling to vibrational modes.

Previous theoretical models have suggested that the transition to Rabi oscillations in a hybrid plexciton system depends on the damping rate of the plasmon mode.^{27,68} We thus investigate the effects of the plasmon damping rate γ on the absorption spectra, with the results shown in Fig. 4. All other simulation parameters are identical to those in Fig. 2 for $\alpha = 0.1$. The most notable effects of γ are on the line width and peak splitting: a smaller plasmon damping rate γ results in larger peak splitting and narrower peaks. A larger damping rate also makes the line shape more asymmetric, resembling the Fano line shape (black curve in the upper panel for $\gamma^{-1} = 3$ fs). These observations are consistent with previous theoretical analyses.^{27,28,69} The effect of coupling to vibrational modes is similar to the results shown in Fig. 3. It reduces the depth of the central dip and slightly alters the ratio of the lower and upper energy peaks, making them more symmetric.

Fig. 5 shows the results obtained by varying the dipole moment of the TLS, μ_{TLS} , while keeping all other parameters the same as in Fig. 2. It is observed that the ratio of the higher to lower energy peaks increases as the dipole moment of the TLS increases, and the position of the central dip redshifts to smaller energies. However, the energy splitting between the two peaks remains almost unchanged. This result is consistent with previous analyses based on the non-Hermitian Hamiltonian model that the width of Rabi splitting is only related to the coupling strength and damping rates.⁶⁹ Since the simulation parameters correspond to a strong coupling case ($\alpha = 0.1$), introducing the coupling of vibrational modes to the TLS (lower panel of Fig. 5) produces effects similar to those in Fig. 4.

C. 2DES

In this subsection, we present results for the 2DES of a TLS coupled to a plasmon mode with varying coupling strengths. We first examine the case of $\alpha = 0.1$, which corresponds to the strong coupling regime. Based on the previous analysis of the effects of vibrational modes on the absorption spectra, we note that these effects are not significant in this regime. We thus focus on the case of a bare TLS coupling the the plasmon mode, and the results are shown in Fig. 6 for various waiting times, T_2 . The calculations are carried out using the method described in Sec. IID, where the laser pulse, as defined in Eq. (21), has a Gaussian profile centered at 15000 cm^{-1} with a full width at half maximum (FWHM) of 4 fs. The spectrum of this pulse is sufficiently broad to cover the entire absorption spectra of the plexciton system.

To better illustrate the dynamical evolution process, we present several representative 2DES at selected waiting times. These times are chosen based on the excited-state population dynamics of the TLS as shown in Fig. 1, and are marked by stars on the green curve (population dynamics for $\alpha = 0.1$). The selected waiting times include the initial time at 0 fs, the first minimum in the population dynamics at approximately 9 fs, the peak near 15 fs, two intermediate times at 4 fs and 12 fs, and a longer waiting time at 36 fs, when the oscillations have decayed.

The 2DES of the plexciton system exhibit distinct features compared to those of an isolated TLS, which shows a single positive peak, or the isolated plasmon mode, where the nonlinear response of the harmonic system is zero. It also differs significantly from the 2DES of a dimer system composed of two coupled TLSs.^{56,70,71} Especially, the diagonal cut of the 2DES reveals prominent negative peaks, which can no longer be directly related to the absorption spectra of the plexciton, as shown in Fig. 2.

During the Rabi oscillation period from $T_2 = 0$ to 15 fs, the 2DES shows a clear “breathing mode” behavior. Along the ω_τ axis, the separation between the two peaks increases from $T_2 = 0$ fs to $T_2 = 4$ fs, reaches its maximum at $T_2 = 9$ fs, and then decreases again to a minimum at $T_2 = 15$ fs. At a longer time, $T_2 = 36$ fs, the 2DES shows a structure similar to the maximum separation observed at $T_2 = 9$ fs. However, due to the rapid decay of the plasmon mode, the amplitude of the 2DES is significantly smaller compared to that at $T_2 = 0$.

We plot in Fig. 7 the evolution of the amplitudes at three points in the ω_τ - ω_t plane, as labeled in Fig. 6: a central point (A) and two points corresponding to the positive (B) and negative (C) peaks. To account for the decay of the overall intensity of the 2DES with increasing T_2 , the amplitudes are normalized to the absolute maximum value of each 2DES. The oscillations of these amplitudes provide further evidence of the Rabi oscillation.

We further simulate the 2DES for a larger coupling strength, $\alpha = 0.2$, with the results presented in Fig. 8. The patterns show a similar behavior to those in Fig. 6, but with a significantly shorter period. The maximum peak separation occurs at $T_2 = 3.8$ fs, followed by a minimum separation at $T_2 = 6.7$ fs. These results confirm that the “breathing mode” pattern observed in the 2DES is indeed associated with the Rabi oscillations of the plexciton system, as presented in Fig. 1 for the population dynamics of the TLS.

The 2DES for the intermediate coupling strength, $\alpha = 0.05$, is shown in Fig. 9, with selected waiting times labeled by blue circles in Fig. 1. At earlier times, there are single positive and negative peaks along the ω_τ direction, even though the absorption spectra in the intermediate coupling regime display double peaks as shown in Fig. 3. This behavior contrasts with the split peak structures observed in the strong coupling regime, as seen in Figs. 6 and 8. Furthermore, no “breathing mode” pattern is observed, which is consistent with the monotonic decay of the population dynamics shown in Fig. 1. At longer times, split peaks appear in the upper positive and central negative regions at $T_2 = 26$ and 32 fs. However, by these waiting times, the amplitude of the 2DES has decreased significantly.

The 2DES in the weak coupling regime with $\alpha = 0.02$ is shown in Fig. 10. Compared to the results in the strong and intermediate coupling regimes, the 2DES occupies a much smaller area in the $\omega_\tau - \omega_t$ plane and shows only single peaks, with the negative peak being more prominent. In addition, the positive peak at smaller ω_t , which is present in the strong and intermediate coupling cases, is also absent in Fig. 10. As the waiting time increases, the initially asymmetric shapes of the positive and negative peaks gradually become more symmetric.

Finally, we investigate the effect of coupling the TLS to intramolecular vibrational modes. The results for $\alpha = 0.1$ and $\alpha = 0.05$ are shown in Figs. 11 and 12, respectively. The parameters for the vibrational mode coupling are the same as those used in Fig. 3. The results show patterns similar to those observed without coupling to the vibrational DOFs, except at longer waiting times. In the strong coupling regime, the “breathing mode” pattern

remains clearly visible, although the beating period is slightly shorter. Additionally, the peak splitting at the longer time, $T_2 = 36.0$ fs, is less pronounced compared to Fig. 6. For the intermediate coupling case shown in Fig. 12, the results are similar to those in Fig. 9, with the exception of the peaks at longer waiting times, $T_2 = 26.0$ fs and 32.0 fs. Here, the positive peak at smaller ω_t is more pronounced than in Fig. 9.

IV. DISCUSSION AND CONCLUSIONS

In summary, we have developed a theoretical model to simulate energy transfer dynamics, absorption spectra, and 2DES for a quantum emitter coupled to a single plasmon mode. The quantum emitter is described using a simplified TLS model. The plasmon mode, due to its Bosonic nature and short lifetime, is treated as a damped harmonic oscillator. Acting as a bath to the TLS, it is further described by a Lorentzian spectral density. The HEOM method is then employed to simulate the dynamics and spectroscopic properties of the coupled TLS-plasmon system over a wide range of parameters.

The absorption spectra of the plexciton system, both without and with the effect of coupling the TLS to intramolecular vibrational modes, are presented. The results indicate that, increasing the TLS-plasmon coupling strength causes the absorption spectra to transition from an asymmetric Fano line shape to a Rabi splitting pattern. Coupling the TLS to intramolecular vibrational DOFs reduces the central dip in the absorption spectra, and results in a more symmetric line shape. In the weak TLS-plasmon coupling regime, this coupling may also suppress the asymmetric Fano resonance feature, and lead to a single absorption peak. Changing the dipole moment of the TLS does not affect the peak splitting, but instead modifies the intensity ratio of the lower and upper peaks.

We have also simulated the 2DES of plexciton systems. The simulated 2DES is markedly different from those of coupled dimers used to study excited-state energy transfer in molecular systems, highlighting the unique features of the nonlinear response in plexciton systems. In the strong TLS-plasmon coupling regime, a “breathing mode” pattern is observed for the split peaks along the ω_τ direction, as a signature of Rabi oscillations. In contrast, the 2DES exhibits individual positive and negative peaks in the intermediate and weak TLS-plasmon coupling regimes, with the peak shapes transitioning from asymmetric to more symmetric as the waiting time increases.

These findings on the 2DES of the plexciton system are consistent with the excited-state population dynamics of the TLS, and suggest that 2DES can be used to investigate energy exchange between the TLS and the plasmon mode. The theoretical model developed in this work provides a foundation for future studies of more complex dynamic behaviors in plexciton systems.^{17,24,72–74}

ACKNOWLEDGMENTS

This work is supported by NSFC (Grant Nos. 21933011, 22203098, and 22433006).

REFERENCES

- ¹Shahbazyan, T. V.; Stockman, M. I. *Plasmonics: theory and applications*; Springer, 2013; Vol. 15.
- ²Tame, M. S.; McEneaney, K.; Özdemir, Ş.; Lee, J.; Maier, S. A.; Kim, M. Quantum plasmonics. **2013**, *9*, 329–340.
- ³Torma, P.; Barnes, W. L. Strong coupling between surface plasmon polaritons and emitters: a review. *Rept. Prog. Phys.* **2014**, *78*, 013901.
- ⁴Li, X.; Zhou, L.; Hao, Z.; Wang, Q.-Q. Plasmon–exciton coupling in complex systems. *Adv. Opt. Mater.* **2018**, *6*, 1800275.
- ⁵Yu, H.; Peng, Y.; Yang, Y.; Li, Z.-Y. Plasmon-enhanced light–matter interactions and applications. *NPJ Comput. Mater.* **2019**, *5*, 45.
- ⁶Xiong, X.; Kongsuwan, N.; Lai, Y.; Png, C. E.; Wu, L.; Hess, O. Room-temperature plexcitonic strong coupling: Ultrafast dynamics for quantum applications. **2021**, *118*.
- ⁷Wang, P.; Krasavin, A. V.; Liu, L.; Jiang, Y.; Li, Z.; Guo, X.; Tong, L.; Zayats, A. V. Molecular plasmonics with metamaterials. *Chem. Rev.* **2022**, *122*, 15031–15081.
- ⁸Kim, Y.; Barulin, A.; Kim, S.; Lee, L. P.; Kim, I. Recent advances in quantum nanophotonics: plexcitonic and vibro-polaritonic strong coupling and its biomedical and chemical applications. *Nanophotonics* **2023**, *12*, 413–439.
- ⁹Luo, Y.; Zhao, J. Plasmon–exciton interaction in colloiddally fabricated metal nanoparticle–quantum emitter nanostructures. *Nano Res.* **2019**, *12*, 2164–2171.

- ¹⁰Purcell, E. M. *Confined Electrons and Photons: New Physics and Applications*; Springer, 1995; pp 839–839.
- ¹¹Zhang, T.; Gao, N.; Li, S.; Lang, M. J.; Xu, Q.-H. Single-particle spectroscopic study on fluorescence enhancement by plasmon coupled gold nanorod dimers assembled on DNA origami. *J. Phys. Chem. Lett.* **2015**, *6*, 2043–2049.
- ¹²Pelton, M. Modified spontaneous emission in nanophotonic structures. *Nat. Photonics* **2015**, *9*, 427–435.
- ¹³Badshah, M. A.; Koh, N. Y.; Zia, A. W.; Abbas, N.; Zahra, Z.; Saleem, M. W. Recent developments in plasmonic nanostructures for metal enhanced fluorescence-based biosensing. *Nanomaterials* **2020**, *10*, 1749.
- ¹⁴Su, Q.; Jiang, C.; Gou, D.; Long, Y. Surface plasmon-assisted fluorescence enhancing and quenching: From theory to application. *ACS Appl. Bio Mater.* **2021**, *4*, 4684–4705.
- ¹⁵Schlather, A. E.; Large, N.; Urban, A. S.; Nordlander, P.; Halas, N. J. Near-field mediated plexcitonic coupling and giant Rabi splitting in individual metallic dimers. *Nano Lett.* **2013**, *13*, 3281–3286.
- ¹⁶Zhao, Q.; Zhou, W.-J.; Deng, Y.-H.; Zheng, Y.-Q.; Shi, Z.-H.; Ang, L. K.; Zhou, Z.-K.; Wu, L. Plexcitonic strong coupling: unique features, applications, and challenges. *J. Phys. D: Appl. Phys.* **2022**, *55*, 203002.
- ¹⁷Zengin, G.; Johansson, G.; Johansson, P.; Antosiewicz, T. J.; Käll, M.; Shegai, T. Approaching the strong coupling limit in single plasmonic nanorods interacting with J-aggregates. *Sci. Rep.* **2013**, *3*, 3074.
- ¹⁸Zengin, G.; Wersäll, M.; Nilsson, S.; Antosiewicz, T. J.; Käll, M.; Shegai, T. Realizing strong light-matter interactions between single-nanoparticle plasmons and molecular excitons at ambient conditions. *Phys. Rev. Lett.* **2015**, *114*, 157401.
- ¹⁹Chikkaraddy, R.; De Nijs, B.; Benz, F.; Barrow, S. J.; Scherman, O. A.; Rosta, E.; Demetriadou, A.; Fox, P.; Hess, O.; Baumberg, J. J. Single-molecule strong coupling at room temperature in plasmonic nanocavities. *Nature* **2016**, *535*, 127–130.
- ²⁰Santhosh, K.; Bitton, O.; Chuntanov, L.; Haran, G. Vacuum Rabi splitting in a plasmonic cavity at the single quantum emitter limit. *Nat. Chem.* **2016**, *7*, ncomms11823.
- ²¹Finkelstein-Shapiro, D.; Mante, P.-A.; Sarisozen, S.; Wittenbecher, L.; Minda, I.; Balci, S.; Pullerits, T.; Zigmantas, D. Understanding radiative transitions and relaxation pathways in plexcitons. *Chem* **2021**, *7*, 1092–1107.

- ²²Peruffo, N.; Mancin, F.; Collini, E. Coherent dynamics in solutions of colloidal plexcitonic nano hybrids at room temperature. *Adv. Opt. Mater.* **2023**, *11*, 2203010.
- ²³González-Tudela, A.; Huidobro, P. A.; Martín-Moreno, L.; Tejedor, C.; García-Vidal, F. Theory of strong coupling between quantum emitters and propagating surface plasmons. *Phys. Rev. Lett.* **2013**, *110*, 126801.
- ²⁴Leng, H.; Szychowski, B.; Daniel, M.-C.; Pelton, M. Strong coupling and induced transparency at room temperature with single quantum dots and gap plasmons. *Nat. Chem.* **2018**, *9*, 4012.
- ²⁵Pelton, M.; Storm, S. D.; Leng, H. Strong coupling of emitters to single plasmonic nanoparticles: exciton-induced transparency and Rabi splitting. *Nanoscale* **2019**, *11*, 14540–14552.
- ²⁶Rudin, S.; Reinecke, T. Oscillator model for vacuum Rabi splitting in microcavities. *Phys. Rev. B* **1999**, *59*, 10227.
- ²⁷Faucheaux, J. A.; Fu, J.; Jain, P. K. Unified theoretical framework for realizing diverse regimes of strong coupling between plasmons and electronic transitions. *J. Phys. Chem. C* **2014**, *118*, 2710–2717.
- ²⁸Manjavacas, A.; García de Abajo, F. J.; Nordlander, P. Quantum plexcitonics: strongly interacting plasmons and excitons. *Nano Lett.* **2011**, *11*, 2318–2323.
- ²⁹Rossi, T. P.; Shegai, T.; Erhart, P.; Antosiewicz, T. J. Strong plasmon-molecule coupling at the nanoscale revealed by first-principles modeling. *Nat. Chem.* **2019**, *10*, 3336.
- ³⁰Kuisma, M.; Rousseaux, B.; Czajkowski, K. M.; Rossi, T. P.; Shegai, T.; Erhart, P.; Antosiewicz, T. J. Ultrastrong coupling of a single molecule to a plasmonic nanocavity: A first-principles study. *ACS photonics* **2022**, *9*, 1065–1077.
- ³¹Bender, C. M. Making sense of non-Hermitian Hamiltonians. *Rep. Prog. Phys.* **2007**, *70*, 947.
- ³²Dzsotjan, D.; Rousseaux, B.; Jauslin, H. R.; des Francs, G. C.; Couteau, C.; Guerin, S. Mode-selective quantization and multimodal effective models for spherically layered systems. *Phys. Rev. A* **2016**, *94*, 023818.
- ³³Varguet, H.; Rousseaux, B.; Dzsotjan, D.; Jauslin, H.; Guérin, S.; Des Francs, G. C. Non-hermitian Hamiltonian description for quantum plasmonics: from dissipative dressed atom picture to Fano states. *J. Phys. B: At. Mol. Phys.* **2019**, *52*, 055404.
- ³⁴Finkelstein-Shapiro, D.; Mante, P.-A.; Balci, S.; Zigmantas, D.; Pullerits, T. Non-Hermitian Hamiltonians for linear and nonlinear optical response: A model for plexcitons.

- J. Chem. Phys.* **2023**, *158*.
- ³⁵Tanimura, Y.; Kubo, R. Time Evolution of a Quantum System in Contact with a Nearly Gaussian-Markoffian Noise Bath. *J. Phys. Soc. Jpn.* **1989**, *58*, 101–114.
- ³⁶Tanimura, Y. Numerically “Exact” Approach to Open Quantum Dynamics: The Hierarchical Equations of Motion (HEOM). *J. Chem. Phys.* **2020**, *153*, 020901.
- ³⁷Yan, Y.; Liu, Y.; Xing, T.; Shi, Q. Theoretical study of excitation energy transfer and nonlinear spectroscopy of photosynthetic light-harvesting complexes using the nonperturbative reduced dynamics method. *Wiley Interdiscip. Rev.: Comput. Mol. Sci.* **2021**, *11*, e1498.
- ³⁸Gelin, M. F.; Egorova, D.; Domcke, W. Efficient method for the calculation of time- and frequency-resolved four-wave mixing signals and its application to photon-echo spectroscopy. *J. Chem. Phys.* **2005**, *123*, 164112.
- ³⁹Garg, A.; Onuchic, J. N.; Ambegaokar, V. Effect of friction on electron transfer in biomolecules. *J. Chem. Phys.* **1985**, *83*, 4491.
- ⁴⁰Tanaka, M.; Tanimura, Y. Quantum Dissipative Dynamics of Electron Transfer Reaction System: Nonperturbative Hierarchy Equation Approach. *J. Phys. Soc. Jpn.* **2009**, *78*, 073802.
- ⁴¹Li, T.; Yan, Y.; Shi, Q. A low-temperature quantum Fokker–Planck equation that improves the numerical stability of the hierarchical equations of motion for the Brownian oscillator spectral density. *J. Chem. Phys.* **2022**, *156*, 064107.
- ⁴²Meier, C.; Tannor, D. Non-Markovian evolution of the density operator in presence of strong laser fields. *J. Chem. Phys.* **1999**, *111*, 3365.
- ⁴³Song, L.-Z.; Shi, Q. A new approach to calculate charge carrier transport mobility in organic molecular crystals from imaginary time path integral simulations. *J. Chem. Phys.* **2015**, *142*, 174103.
- ⁴⁴Xu, M.; Yan, Y.; Shi, Q.; Ankerhold, J.; Stockburger, J. Taming quantum noise for efficient low temperature simulations of open quantum systems. *Phys. Rev. Lett.* **2022**, *129*, 230601.
- ⁴⁵Dan, X.; Xu, M.; Stockburger, J.; Ankerhold, J.; Shi, Q. Efficient low-temperature simulations for fermionic reservoirs with the hierarchical equations of motion method: Application to the Anderson impurity model. *Phys. Rev. B* **2023**, *107*, 195429.
- ⁴⁶Shi, Q.; Chen, L.-P.; Nan, G.-J.; Xu, R.-X.; Yan, Y.-J. Electron Transfer Dynamics: Zusman Equation Versus Exact Theory. *J. Chem. Phys.* **2009**, *130*, 164518.

- ⁴⁷Zhu, L.; Liu, H.; Xie, W.; Shi, Q. Explicit system-bath correlation calculated using the hierarchical equations of motion method. *J. Chem. Phys.* **2012**, *137*, 194106.
- ⁴⁸Liu, H.; Zhu, L.; Bai, S.; Shi, Q. Reduced Quantum Dynamics with Arbitrary Bath Spectral Densities: Hierarchical Equations of Motion Based on Several Different Bath Decomposition Schemes. *J. Chem. Phys.* **2014**, *140*, 134106.
- ⁴⁹Zhang, H.-D.; Qiao, Q.; Xu, R.-X.; Yan, Y.-J. Solvent-induced polarization dynamics and coherent two-dimensional spectroscopy: Dissipaton equation of motion approach. *Chem. Phys.* **2016**, *581*, 237–244.
- ⁵⁰Chen, Z.-H.; Wang, Y.; Xu, R.-X.; Yan, Y. Correlated vibration-solvent effects on the non-Condon exciton spectroscopy. *J. Chem. Phys.* **2021**, *154*, 244105.
- ⁵¹Mukamel, S. *Principles of Nonlinear Optical Spectroscopy*; Oxford: New York, 1995.
- ⁵²Chen, L.-P.; Zheng, R.-H.; Shi, Q.; Yan, Y.-J. Optical Line Shapes of Molecular Aggregates: Hierarchical Equations of Motion Method. *J. Chem. Phys.* **2009**, *131*, 094502.
- ⁵³Jing, Y.; Chen, L.; Bai, S.; Shi, Q. Equilibrium excited state and emission spectra of molecular aggregates from the hierarchical equations of motion approach. *J. Chem. Phys.* **2013**, *138*, 045101.
- ⁵⁴Seidner, L.; Stock, G.; Domcke, W. Nonperturbative Approach to Femtosecond Spectroscopy: General Theory and Application to Multidimensional Nonadiabatic Photoisomerization Processes. *J. Chem. Phys.* **1995**, *103*, 3998–4011.
- ⁵⁵Gelin, M. F.; Egorova, D.; Domcke, W. Efficient calculation of time- and frequency-resolved four-wave-mixing signals. *Acc. Chem. Res.* **2009**, *42*, 1290–1298.
- ⁵⁶Leng, X.; Yue, S.; Weng, Y.-X.; Song, K.; Shi, Q. Effects of finite laser pulse width on two-dimensional electronic spectroscopy. *Chem. Phys. Lett.* **2017**, *667*, 79–86.
- ⁵⁷Wang, Y.; Pan, Z. J.; Zhang, H.-D.; Yan, Y. J. Dissipaton dynamics theory versus quantum master equations. *Chem. Phys.* **2018**, *515*, 94–101.
- ⁵⁸Tan, H.-S. Theory and phase-cycling scheme selection principles of collinear phase coherent multi-dimensional optical spectroscopy. *J. Chem. Phys.* **2008**, *129*.
- ⁵⁹Yan, S.; Tan, H.-S. Phase cycling schemes for two-dimensional optical spectroscopy with a pump-probe beam geometry. *Chem. Phys.* **2009**, *360*, 110–115.
- ⁶⁰Egorova, D.; Gelin, M. F.; Domcke, W. Analysis of cross peaks in two-dimensional electronic photon-echo spectroscopy for simple models with vibrations and dissipation. *J. Chem. Phys.* **2007**, *126*, 074314.

- ⁶¹Cheng, Y.-C.; Engel, G. S.; Fleming, G. R. Elucidation of population and coherence dynamics using cross-peaks in two-dimensional electronic spectroscopy. *Chem. Phys.* **2007**, *341*, 285–295.
- ⁶²Leng, X.; Yan, Y.-M.; Zhu, R.-D.; Song, K.; Weng, Y.-X.; Shi, Q. Simulation of the two-dimensional electronic spectroscopy and energy transfer dynamics of light-harvesting complex II at ambient temperature. *J. Phys. Chem. B* **2018**, *122*, 4642–4652.
- ⁶³Hamm, P.; Zanni, M. *Concepts and methods of 2D infrared spectroscopy*; Cambridge University Press, 2011.
- ⁶⁴Cheng, Y.-C.; Fleming, G. R. Coherence quantum beats in two-dimensional electronic spectroscopy. *J. Phys. Chem. A* **2008**, *112*, 4254–4260.
- ⁶⁵Novotny, L. Strong coupling, energy splitting, and level crossings: A classical perspective. *Am. J. Phys.* **2010**, *78*, 1199–1202.
- ⁶⁶Hümmer, T.; García-Vidal, F.; Martín-Moreno, L.; Zueco, D. Weak and strong coupling regimes in plasmonic QED. *Phys. Rev. B* **2013**, *87*, 115419.
- ⁶⁷Adato, R.; Artar, A.; Erramilli, S.; Altug, H. Engineered absorption enhancement and induced transparency in coupled molecular and plasmonic resonator systems. *Nano Lett.* **2013**, *13*, 2584–2591.
- ⁶⁸Yang, X.; Wodtke, A. M. Surface reaction dynamics. *Chem. Soc. Rev.* **2016**, *45*, 3573–3575.
- ⁶⁹Baranov, D. G.; Wersall, M.; Cuadra, J.; Antosiewicz, T. J.; Shegai, T. Novel nanostructures and materials for strong light–matter interactions. *Acs Photonics* **2018**, *5*, 24–42.
- ⁷⁰Chen, L.-P.; Zheng, R.-H.; Shi, Q.; Yan, Y.-J. Two-Dimensional Electronic Spectra from the Hierarchical Equations of Motion Method: Application to Model Dimers. *J. Chem. Phys.* **2010**, *132*, 024505.
- ⁷¹Gelzinis, A.; Augulis, R.; Butkus, V.; Robert, B.; Valkunas, L. Two-dimensional spectroscopy for non-specialists. *Biochimica et Biophysica Acta (BBA)-Bioenergetics* **2019**, *1860*, 271–285.
- ⁷²Balci, S. Ultrastrong plasmon–exciton coupling in metal nanoprisms with J-aggregates. *Opt. Lett.* **2013**, *38*, 4498–4501.
- ⁷³Groß, H.; Hamm, J. M.; Tufarelli, T.; Hess, O.; Hecht, B. Near-field strong coupling of single quantum dots. *Sci. Adv.* **2018**, *4*, eaar4906.
- ⁷⁴Bitton, O.; Gupta, S. N.; Haran, G. Quantum dot plasmonics: from weak to strong coupling. *Nanophotonics* **2019**, *8*, 559–575.

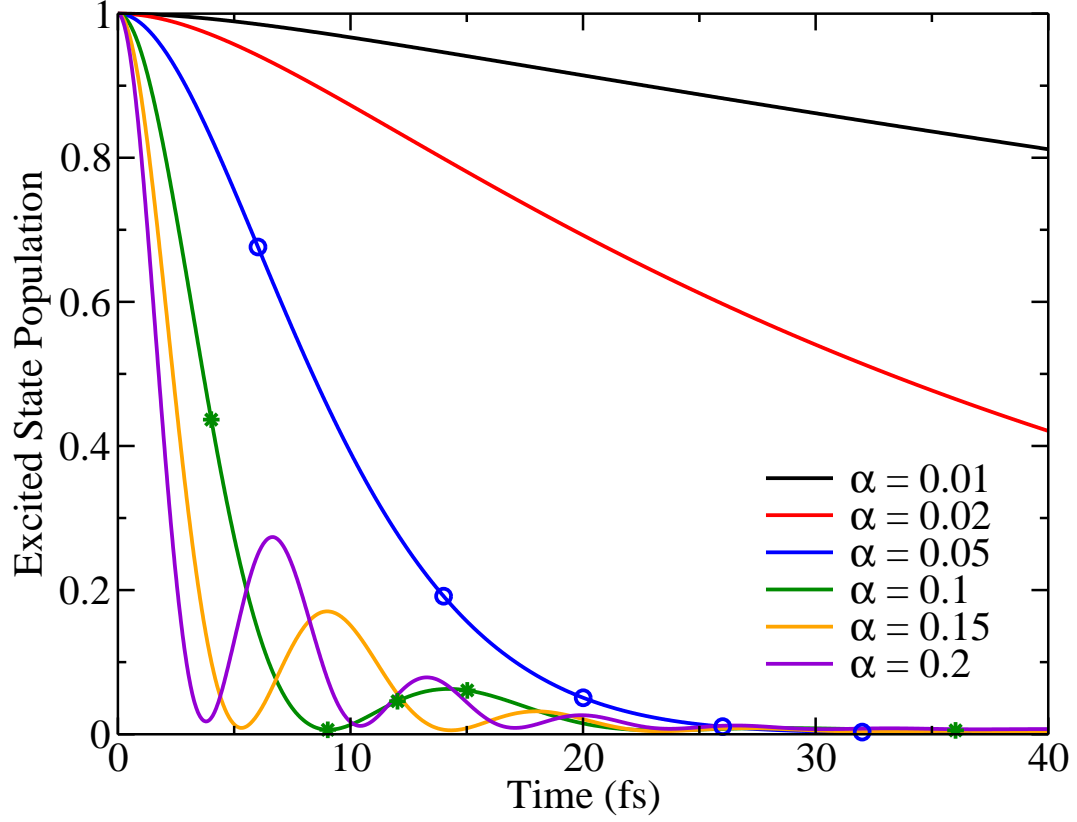


FIG. 1. Excited state population dynamics of the TLS with different TLS-plasmon coupling strengths. The initial state is a factorized state with the TLS in the excited state and the plasmon mode in the thermal equilibrium. Marked symbols on the blue and green curves are used in the later 2DES simulations.

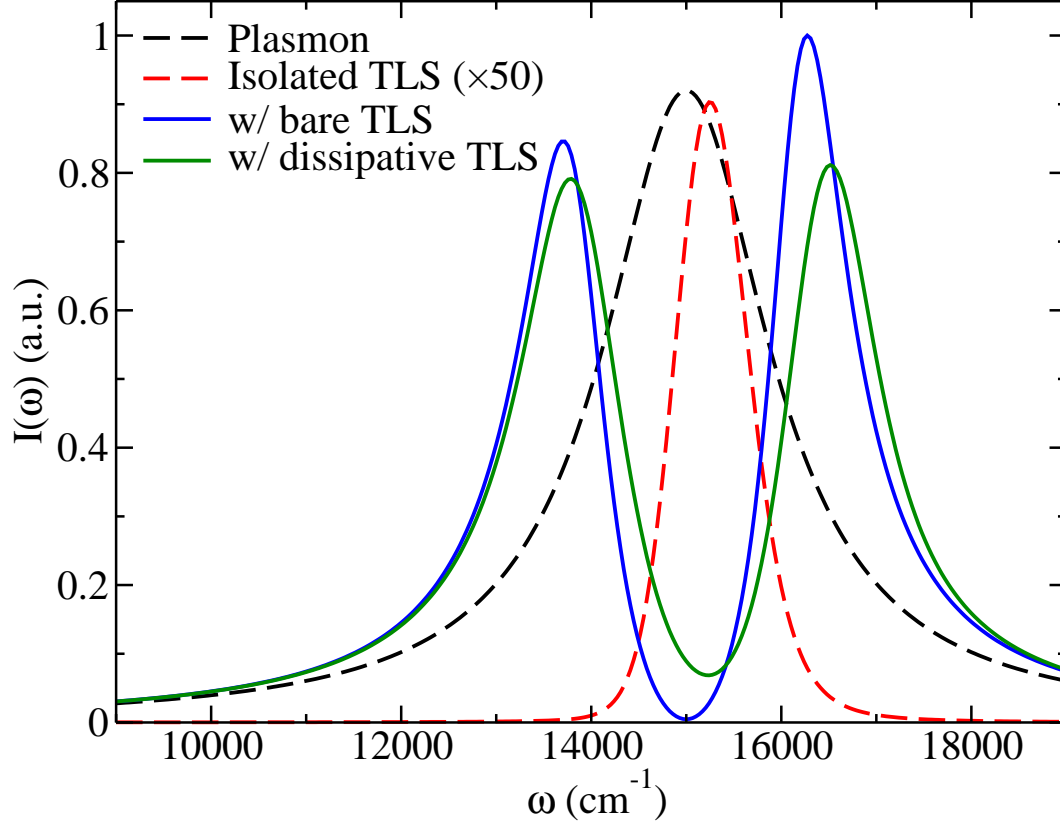


FIG. 2. Linear absorption spectra of the plasmon mode (black dashed line), an isolated TLS with coupling to the vibrational DOFs described by a Debye-Drude spectral density (red dashed line), the bare TLS coupled to the plasmon mode (blue solid line), and the TLS coupled simultaneously to the plasmon mode and vibrational DOFs (green solid line). The red line is rescaled by 50 times for better visualization.

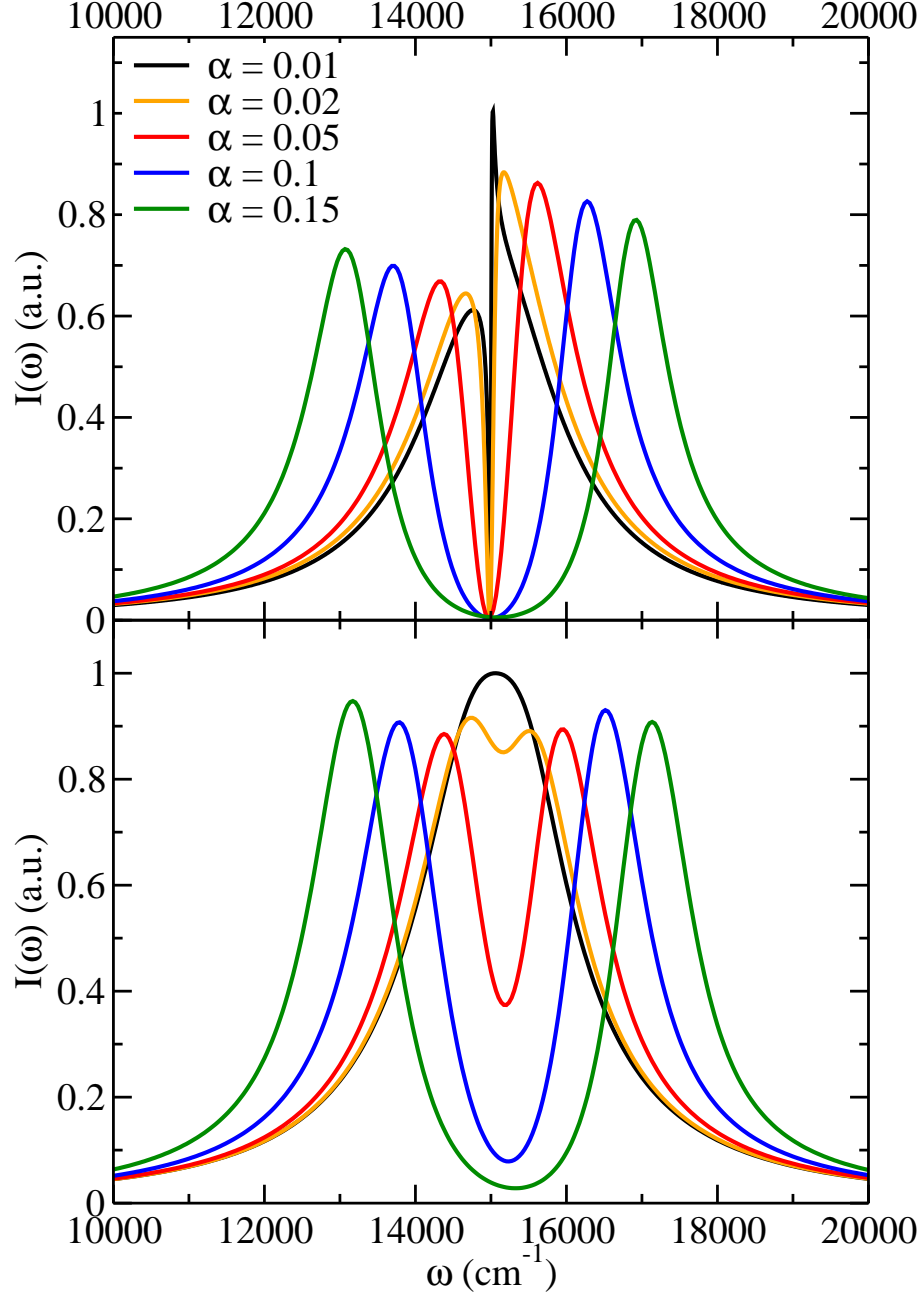


FIG. 3. The absorption spectra of the plexciton system with different coupling strength α . The upper panel shows the spectra of the bare TLS coupled to the plasmon mode, and the lower panel shows results of a TLS coupled simultaneously to the plasmon mode and vibrational DOFs. All the other parameters are the same as those in Fig. 2.

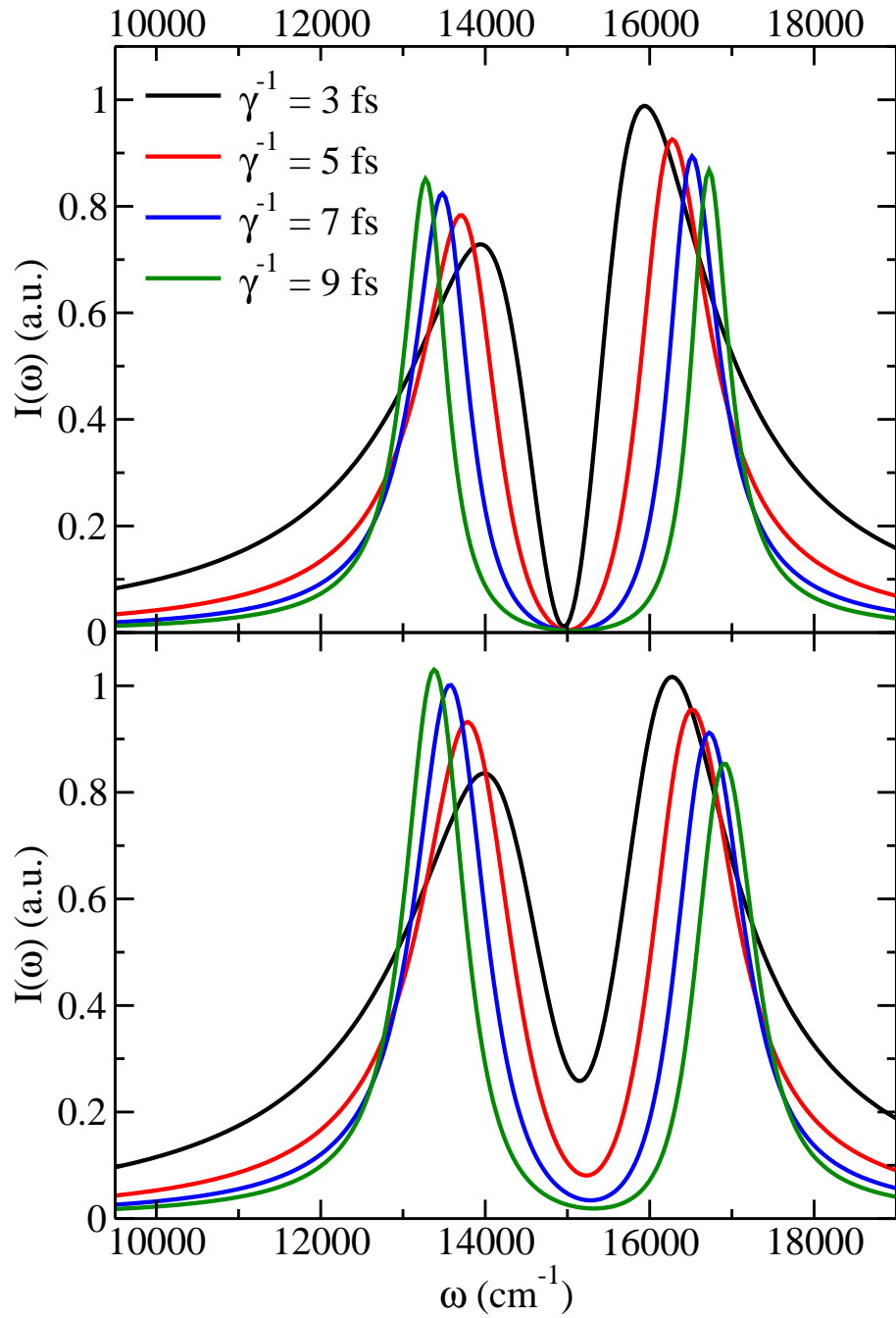


FIG. 4. Same as Fig. 3, for different plasmon mode relaxation rate γ .

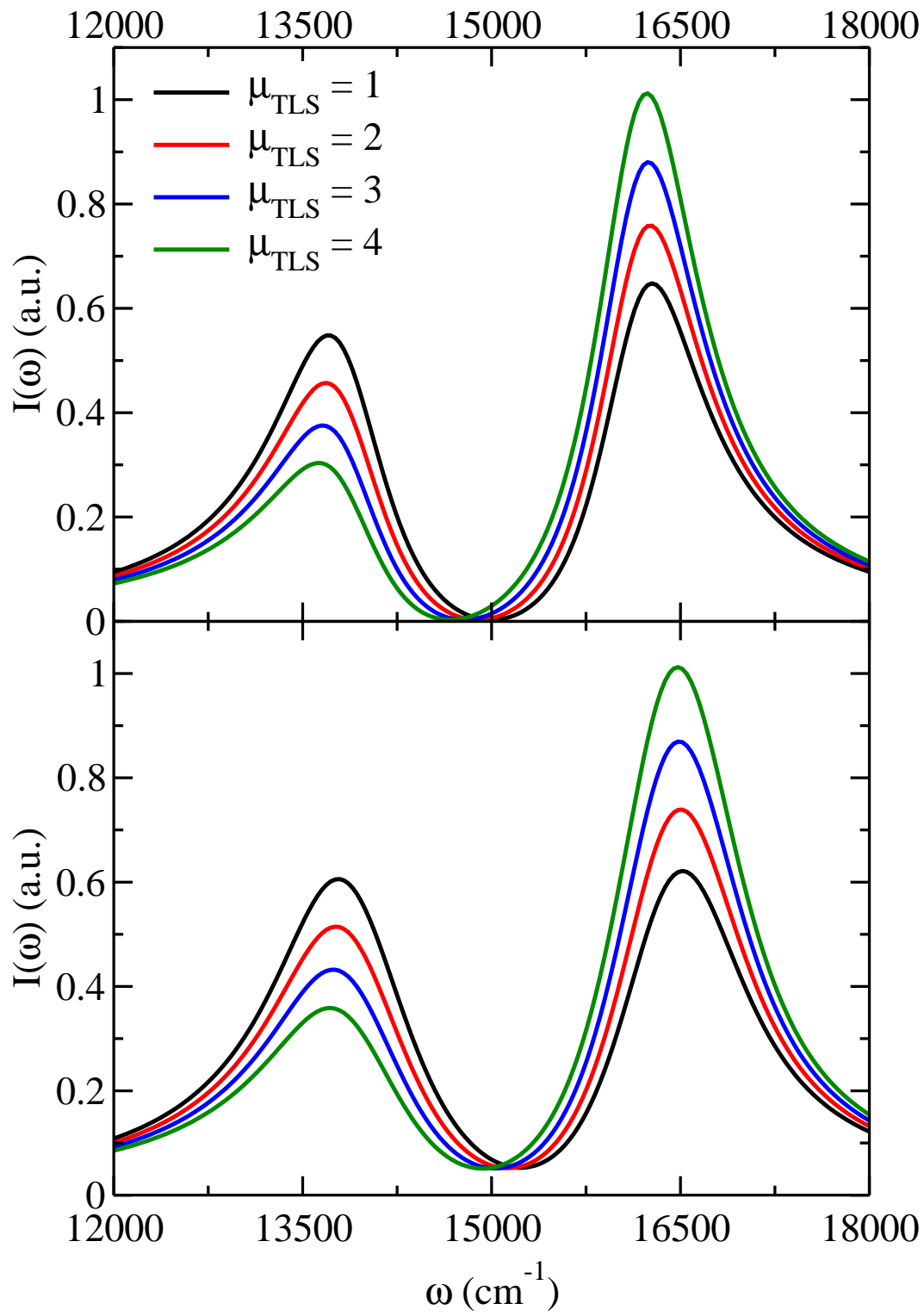


FIG. 5. Same as Fig. 3, for different TLS transition dipole moment μ_{TLS} .

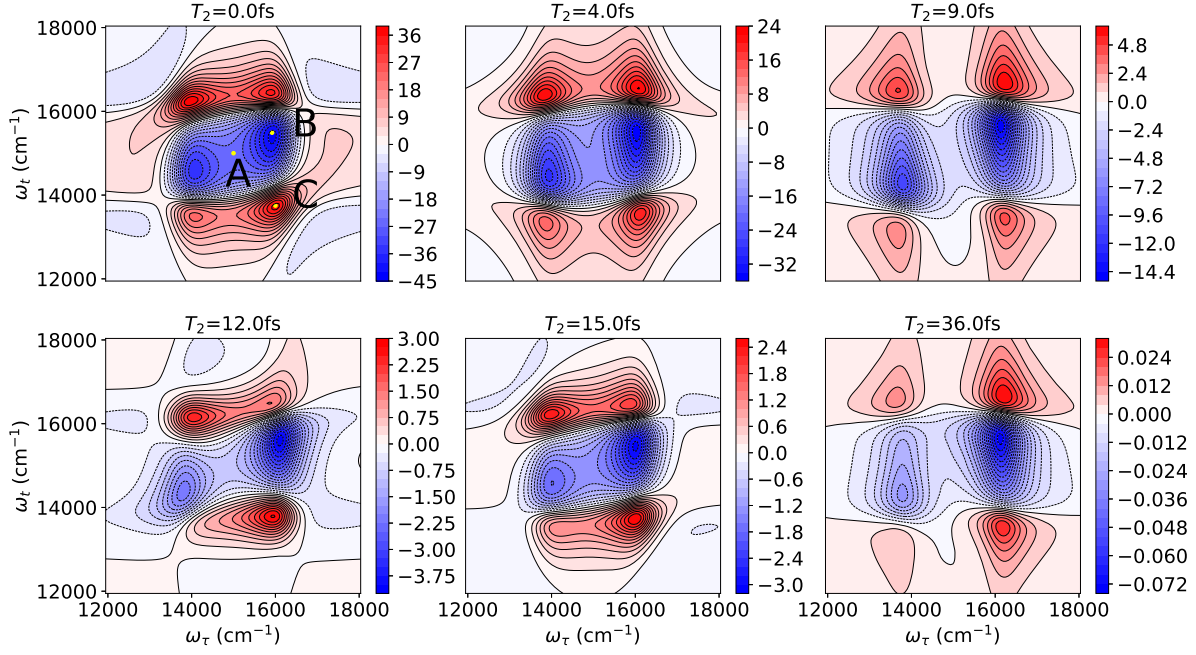


FIG. 6. Simulated 2DES of a bare TLS coupled to the plasmon mode at different waiting time T_2 for the strong coupling case $\alpha = 0.1$. All the other parameters are the same as those in Fig. 2.

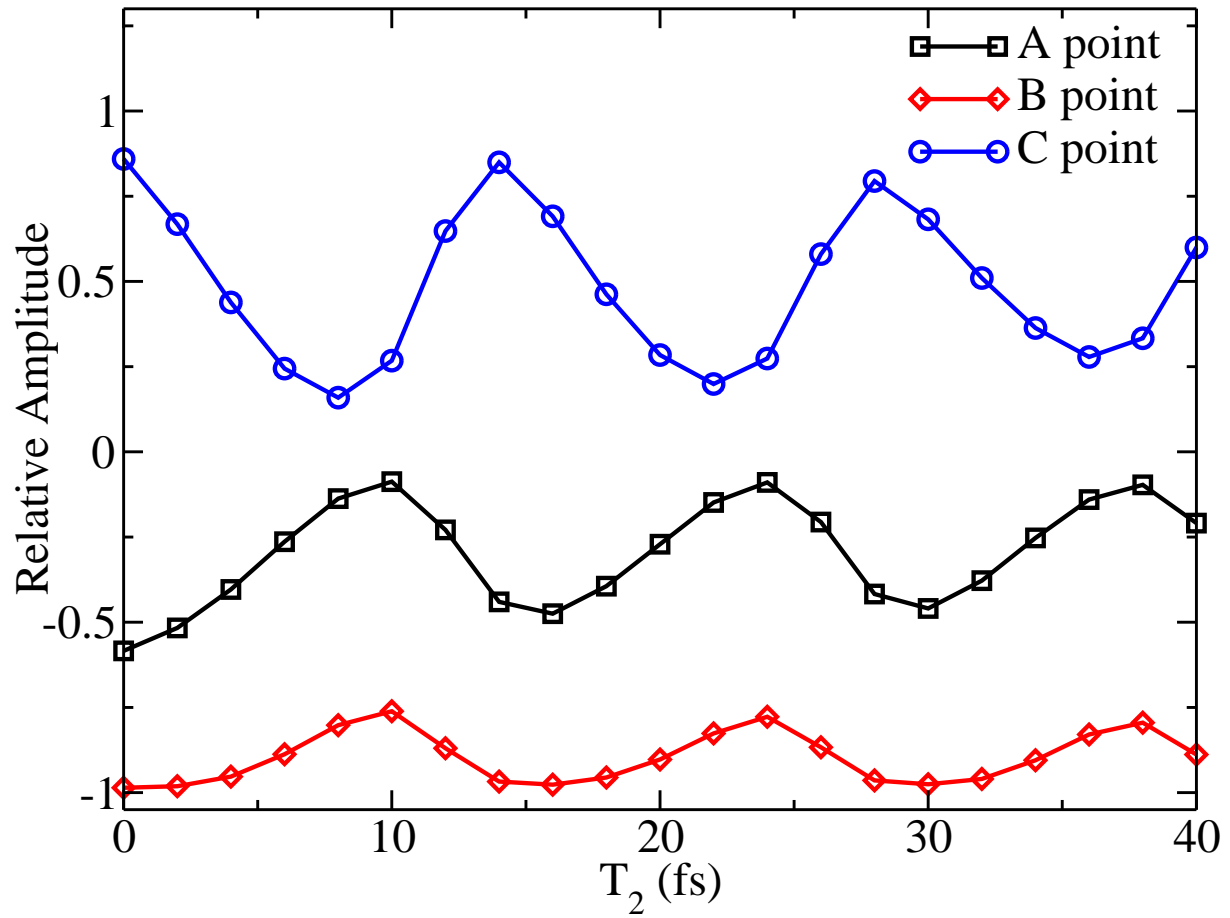


FIG. 7. Time evolution of the relative amplitudes at three selected points in the $\omega_\tau - \omega_t$ plane as labeled in Fig. 6.

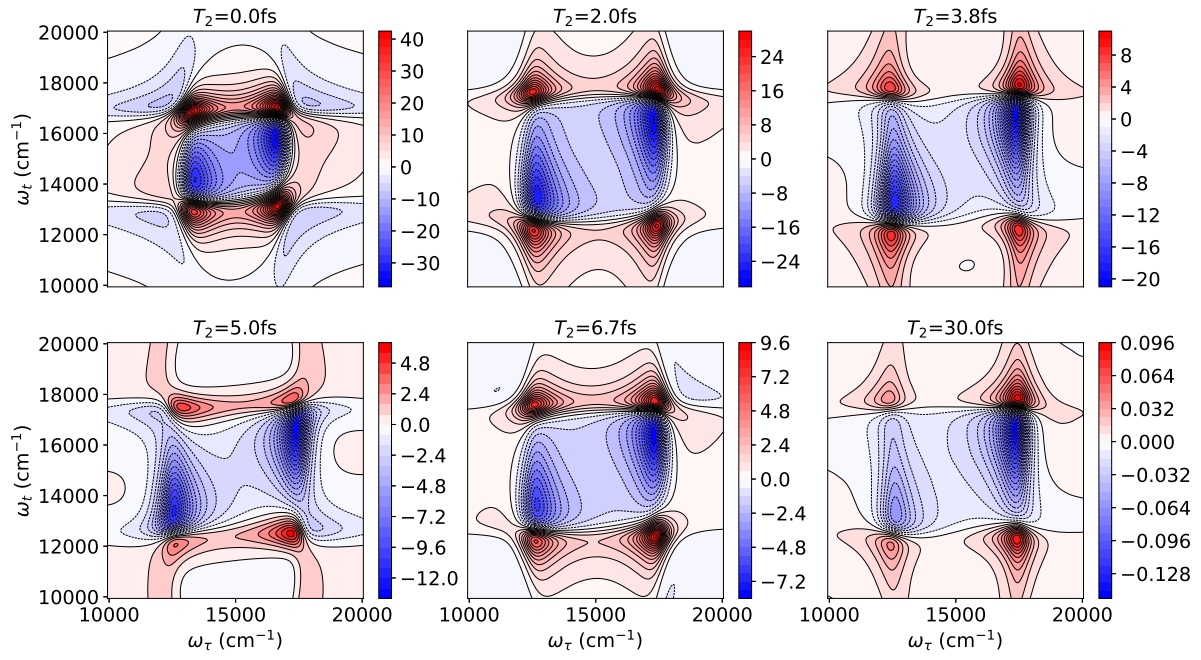


FIG. 8. Same as Fig. 6 for $\alpha = 0.2$.

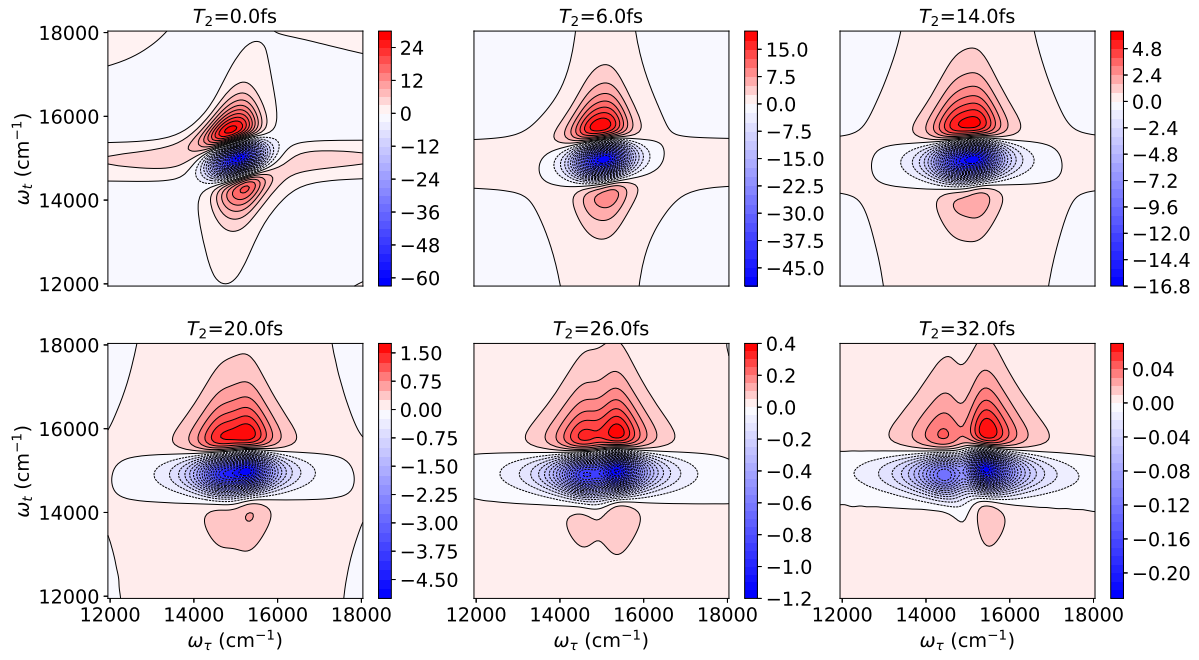


FIG. 9. Same as Fig. 6 for the intermediate coupling case $\alpha = 0.05$.

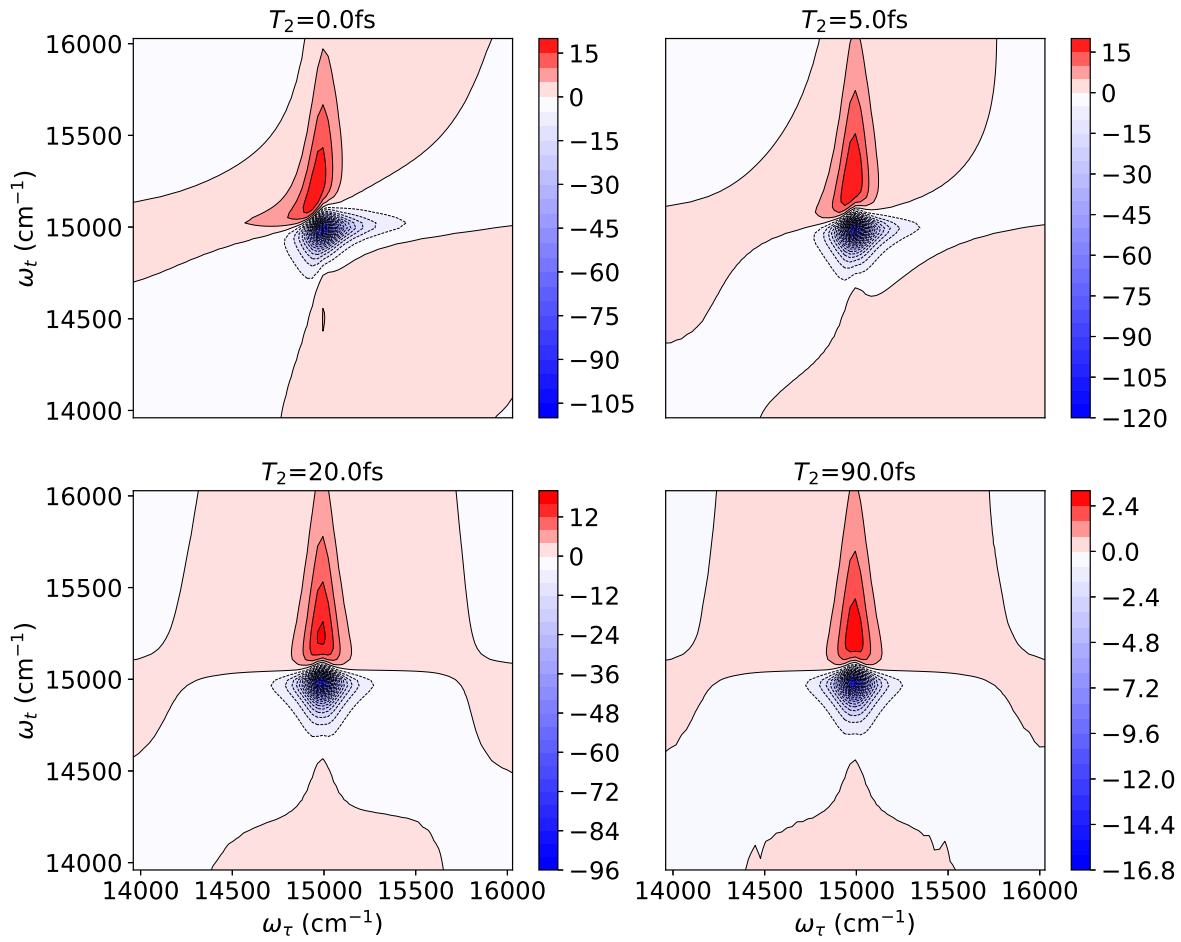


FIG. 10. Same as Fig. 6 for the weak coupling case $\alpha = 0.02$.

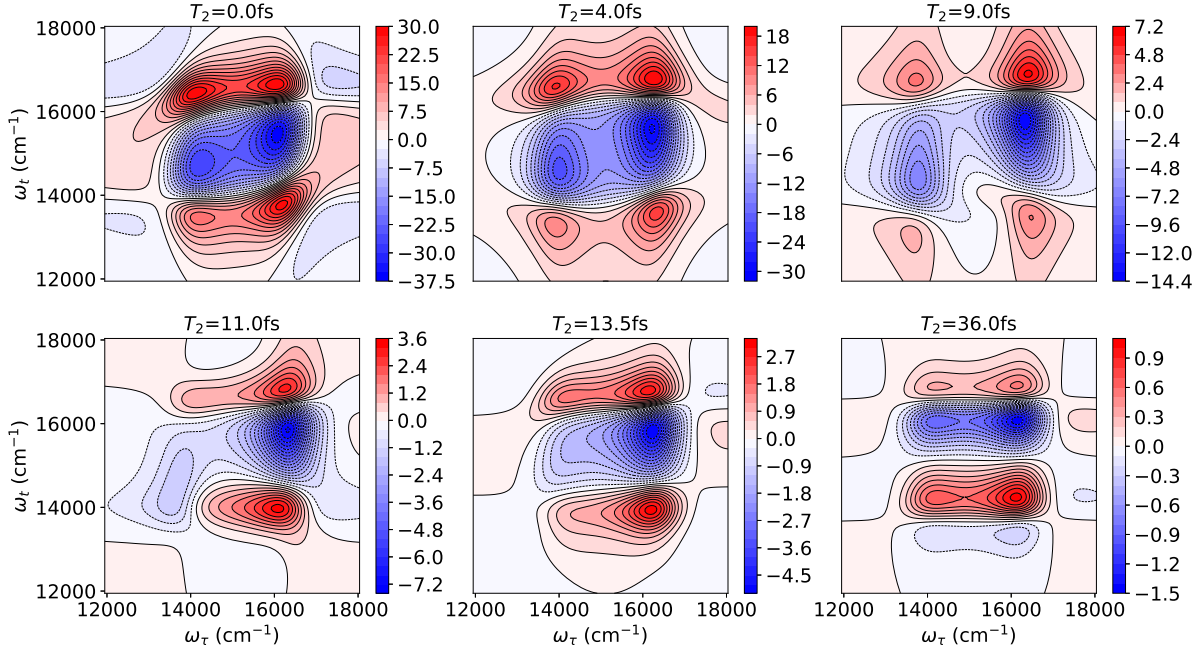


FIG. 11. Simulated 2DES of a TLS coupled simultaneously to the plasmon mode and intramolecular vibrational DOFs for the strong coupling case $\alpha = 0.1$. All the other parameters are the same as those in Fig. 6.

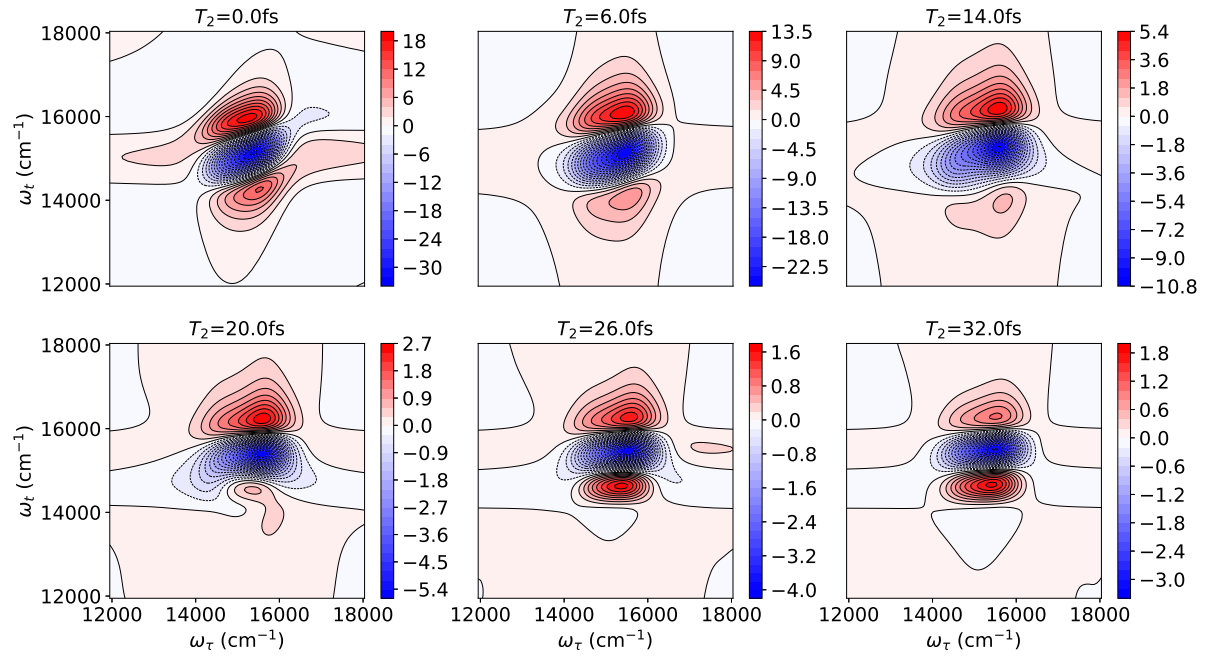


FIG. 12. Same as Fig. 11 for the intermediate coupling case $\alpha = 0.05$.